Journal of Environmental Chemical Engineering 13 (2025) 115439

Contents lists available at ScienceDirect

Journal of Environmental Chemical Engineering

journal homepage: www.elsevier.com/locate/jece

Promotion mechanism of SO_2 on the catalytic oxidation of NO by H_2O_2

Zhengyang Gao [a,b], Yixiao Sun [a,b], Ziwei Miao [a,b], Yuanzheng Qu [a,b], Xiang Li [a,b], Shilong Chen [a,b], Weijie Yang [a,b,*]

[a] Department of Power Engineering, North China Electric Power University, Baoding, Hebei 071003, China
[b] Hebei Key Laboratory of Low Carbon and High-Efficiency Power Generation Technology, North China Electric Power University, Baoding, Hebei 071003, China

ARTICLE INFO

Keywords:
SO_2
NO oxidation
H_2O_2
Single-atom catalyst
Density functional theory

ABSTRACT

The efficiency of advanced oxidation process based on H_2O_2 for NO removal is depended on the gas atmosphere. SO_2 significantly enhances NO oxidation by H_2O_2 over various catalysts. To reveal this important mechanism, single-atom catalysts (SACs) with uniform and well-defined active site is selected as the model catalyst. Combining fixed-bed experiments and density functional theory (DFT) calculations, the promotion mechanism of SO_2 on catalytic oxidation of NO over SACs by H_2O_2 is illustrated through analyzing gas adsorption characteristics, reaction paths and energy barriers. In fact, SO_2 plays a catalytic role in the processes of H_2O_2 oxidizing NO through the following reaction equations ($SO_2 + \bullet OH \rightarrow HSO_3$; $HSO_3 + NO \rightarrow SO_2 + HNO_2$). SO_2 can accelerate the reaction cycle through transforming the desorption of products, which can significantly reduce the energy barrier from 0.98 eV (HNO_2 desorption, without SO_2) to 0.3 eV (SO_2 desorption, with SO_2). Due to the smaller charge transfer between SACs and gaseous, the adsorption energy of SO_2 is lower than that of HNO_2. This work provides new insights into the promotion micro-mechanism of SO_2 on NO oxidation over different catalysts, which is of great interests for developing industrial catalysts.

1. Introduction

Advanced oxidation processes (AOPs) as a promising solution to improve the removal of contaminants have garnered significant attention in recent years [1,2]. These techniques use the potential of vaporized hydrogen peroxide (H_2O_2), an economical and eco-friendly oxidant, to facilitate the conversion of water-insoluble NO into water-soluble NO_x species [3,4]· H_2O_2 comprises of hydrogen and oxygen, and its decomposition produces only water and oxygen at room temperatures [5–8]. Furthermore, the activation of H_2O_2 generates intermediate free radicals that possess formidable oxidizing capabilities. This unique property underscores its effectiveness in enhancing NO removal efficiency, thereby making AOPs a compelling choice for solving air pollution problems.[9–11]

While SO_2 is inherently more easily removed due to its high solubility in water, its impact on the oxidation of NO by H_2O_2 remains a subject of debate [12–15]. Numerous past investigations have revealed that SO_2 can promote the oxidation of NO by H_2O_2 [16–19]. Obviously, SO_2 exert distinct influences on the removal efficiency of NO across different catalysts ($Fe_2(SO_4)_3$ [20], $Fe/Al_2O_3@SiO_2$ [21], nanoscale zerovalent iron (nZVI) [22], Fe/Al_2O3 [21], $Fe_2(Mo_4)_3$ [17,23], Modified Fly Ash [24], $Fe_{2.5}M_{0.5}O_4$ (M = Fe, Mn, Ti and Cu) [25], Activated Fly Ash (AFA) [26], and $Cu\text{-}Fe/TiO_2$ [27]) as shown in Fig. 1. Zhao et al. employed a highly efficient nanoscale zerovalent iron (nZVI) [22] to activate vaporized H_2O_2 for NO removal, achieving an impressive 80.4 % NO conversion rate. Intriguingly, upon elevating the SO_2 concentration, the NO conversion rate further escalated to 88.4 %. Wu et al. conducted an experiment utilizing solid-phase $Fe_2(SO_4)_3$ [20] as a catalyst for NO removal by H_2O_2. To clarify the role of SO_2 in this process, they employed XPS analysis and found that the presence of SO_2 enhances the NO removal rate to 92.5 %, a significant improvement over the 80 % achieved without SO_2. Jia et al. crafted Fe/Al_2O_3 and $Fe/Al_2O_3@SiO_2$ [21] two distinct catalysts and discovered that both exhibited enhanced NO removal capabilities when exposed to SO_2. Detailed information is shown in Table S1. In conclusion, SO_2 is important factors influencing the oxidation of NO by AOPs. However, there exists a significant gap in the comprehension of microscopic mechanisms underlying how SO_2 influences the oxidation of NO by H_2O_2 [28,29]. It is imperative to promptly embark on related research endeavors.

For catalysts with many active sites, such as $Fe_2(SO_4)_3$ [20], the adsorption of gas molecules in the catalyst is very complex [30]·H_2O_2 activates to produce different free radicals (O•, •OH, and HO_2•) at

---

* Corresponding author at: Department of Power Engineering, North China Electric Power University, Baoding, Hebei 071003, China.
E-mail address: yangwj@ncepu.edu.cn (W. Yang).

https://doi.org/10.1016/j.jece.2025.115439
Received 14 November 2024; Received in revised form 27 December 2024; Accepted 12 January 2025

different adsorption sites [31,32]. Furthermore, the presence of oxygen in various electronic states within some catalysts also affect the oxidation of NO by H_2O_2 [33–35]. Given these convoluted and challenging-to-quantify factors, there arises a pressing need for a model catalyst featuring a solitary active center [36]. Such a catalyst would serve as a pivotal tool in unraveling the intricate mechanism through which SO_2 modulates the oxidation of NO by H_2O_2 [37]. In recent times, single-atom catalysts (SACs) have garnered significant attention due to their selectivity and stability [38–40]. SO_2 is an important pollutant in flue gas, but many catalysts are prone to sulfur poisoning, resulting in catalyst deactivation [41–45]. Graphene, renowned for its robust sulfur resistance, emerges as an ideal substrate to safeguard against catalyst contamination and ensure continuous activity [46–48]. By incorporating Fe as the active site, these graphene-based SACs utilize the capability of H_2O_2 to generate free radicals, thereby enhancing its oxidative efficiency [49]. Furthermore, previous studies have demonstrated the good catalytic performance of graphene-supported single-atom iron catalysts ($Fe\text{-}N_4\text{-}C$) in the removal of pollutants like NO and Hg, underscoring their potential in addressing environmental challenges [50–53].

In this work, we delve into the influence of SO_2 on the catalytic oxidation of NO by H_2O_2 over $Fe\text{-}N_4\text{-}C$, using NO oxidation experiment and spin-polarized DFT calculations (ISPIN=2 in VASP INCAR), augmented with van der Waals corrections (DFT-D3) [54]. Firstly, our experimental findings reveal that the presence of SO_2 on $Fe\text{-}N_4\text{-}C$ significantly enhances NO removal efficiency. Subsequently, $Fe\text{-}N_4\text{-}C$ was used as a model catalyst to computationally analyze the adsorption behavior of diverse sulfides on its surface. Through further calculations, the mechanism of SO_2 affecting the activation of H_2O_2 on $Fe\text{-}N_4\text{-}C$ is revealed. Next, we simulated and calculated the reaction pathways and energy barriers (E_b) associated with the formation of sulfides and the oxidation of NO. Finally, through analyzing and comparing the reactions process of different sulfides to oxidize NO, we conclude that SO_2 can promote the oxidation of NO by H_2O_2. This comprehensive exploration deepens our understanding of the role of SO_2 in promoting the catalytic oxidation of NO by H_2O_2 on the catalyst.

2. Materials and methods

2.1. Materials

Iron nitrate nonahydrate (Fe $(NO_3)_3\cdot 9\ H_2O$) and 2-methylimidazole were purchased from Shanghai Macklin Biochemical Technology Co., Ltd. Zinc nitrate hexahydrate (Zn $(NO_3)_2\cdot 6\ H_2O$) and methanol anhydrous were purchased from Tianjin Kemiou Chemical Reagent Co., Ltd. These chemicals were used as received without further purification. Deionized water was acquired from a water purification machine.

2.2. Preparation and characterization of the catalysts

The preparation of $Fe\text{-}N_4\text{-}C$ requires zeolite imidazole skeleton (ZIF-8) as the precursor. Firstly, Zn $(NO_3)_2\cdot 6\ H_2O$ (3.39 g), Fe $(NO_3)_3\cdot 9\ H_2O$ (100 mg) and 2-methylimidazole (3.93 g) were fully dissolved with 200 mL of methanol [55–57]. Then, the mixed solution was heated in an oil bath at 60 °C and stirred magnetically for 24 hours. After cooling to room temperature, the samples were centrifuged 3 times and dried, ground into powder to obtain Fe-ZIF-8 precursor containing doped metal. Finally, the powder was pyrolyzed in an N_2 atmosphere heated to 900 °C at an accelerated rate of 5 °C/min for 2 h to synthesize $Fe\text{-}N_4\text{-}C$.

Crystal structure was measured by powder X-ray diffraction (XRD) patterns using a Smartlab SE diffractometer with monochromatic Co Kα radiation of 1.78897 Å wavelength at 40 kV and 40 mA. The 2θ in the range of 5–85°. The catalyst morphology was observed by a Talos F200S G2 microscope transmission electron microscopy (TEM). The Fe K-edge X-ray absorption near edge structure (XANES) and extended X-ray absorption fine structure (EXAFS) experiments were carried out at 1W1B station in Beijing Synchrotron Radiation Facility (BSRF) at ambient conditions. The obtained XAFS data was extracted and processed following standard procedures using IFEFFIT software and Athena module.

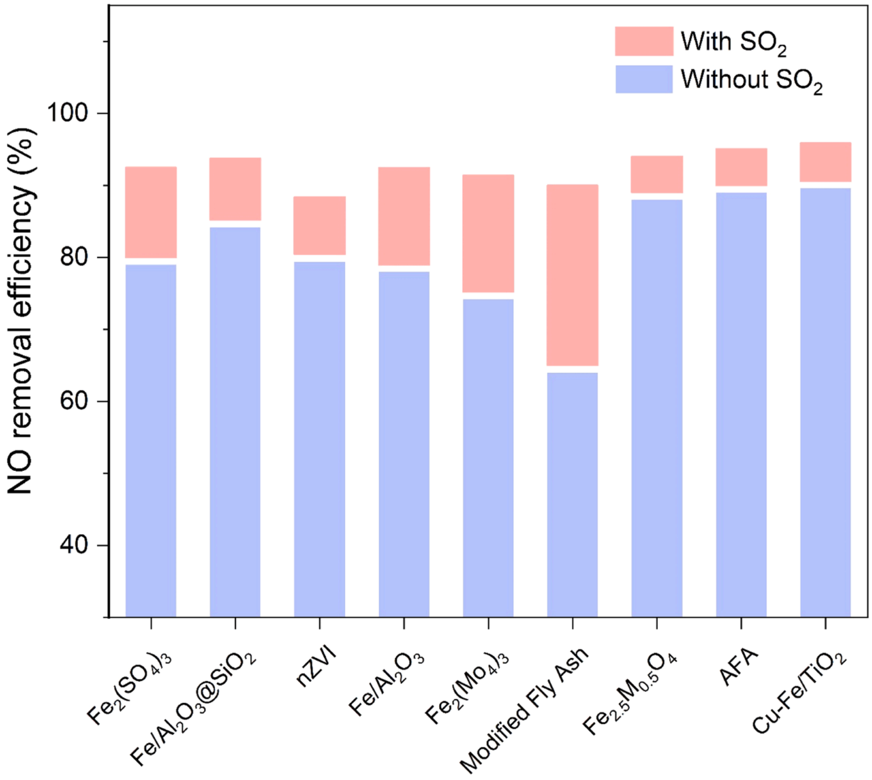

Fig. 1. NO removal efficiency of different catalysts.

2.3. Catalytic evaluation

Fig. 2 shows the experimental apparatus for removal of NO. The system consisted of: (1) simulated flue gas generation system, (2) vaporized H_2O_2 generation system, (3) catalytic oxidation system, (4) drying system and (5) measure system. The simulated flue gas system comprised N_2, NO, SO_2, and O_2 from compressed gas cylinders and four mass flow controllers (Beijing Huacheng Electronics Co., Ltd). The total flow rate of the simulated flue gas is 1 L/min, O_2 content is 6 %, and the concentration of NO and SO_2 is 500 ppm. The vaporized H_2O_2 generation system was composed of a peristaltic pump (YZ1515 Baoding QiLi Precision pump Co., Ltd) and an electric heating jacket. The catalytic oxidation system consists of a quartz tube, an electric furnace, and a temperature control device. The drying system consisted of 2 separate scrubbing cylinders, one filled with purified water and one anhydrous $CaCl_2$. The systems are connected by Teflon tubing, all of which are wrapped with a heat trace (140 °C) to avoid condensation of H_2O_2 vapor. The peristaltic pump delivered a hydrogen peroxide solution (3 wt%) into the electric heating jacket at a flow rate of 250 μL/min for the vaporization of H_2O_2, and the quartz tube was heated to 140 °C by an electric heating furnace. Using N_2 as the carrier gas, H_2O_2 steam and simulated flue gas were fed into a quartz tube reactor (diameter 10 mm, length 300 mm). The catalyst was put into the quartz tube and the quartz wool was inserted into the two sections to fix, with a catalyst amount of 0.1 g. The distance between the top of the reactor and the catalyst section is 150 mm, ensuring that the catalyst can fully contact with the mixed gas to react. To accurately measure the concentration of NO, the reaction gas is dried by anhydrous $CaCl_2$, and the composition and concentration of the outlet flue gas are analyzed by a gas analyzer (MRU). The removal efficiency of NO (η) is calculated according to the equation:

$$\eta(\%) = \frac{C_{inlet} - C_{outlet}}{C_{inlet}} \times 100\%$$

where C_{inlet} is the inlet concentration of NO; and C_{outlet} is the outlet concentration of NO.

2.4. DFT calculation

In this study, all Density Functional Theory (DFT) calculations were meticulously conducted with the assistance of the Vienna Ab initio Simulation Package (VASP) [58,59]. The projector augmented wave (PAW) method was employed for these computations, ensuring a robust framework for the analysis. To accurately handle exchange-correlated interactions, we leveraged Generalized Gradient Approximation (GGA) methods, specifically the Perdew-Burke-Ernzerhof (PBE) functional [60]. To further enhance the precision and rationality of the optimized structures, the DFT-D3 framework was adopted, incorporating the vital consideration of van der Waals forces into the interaction dynamics [61,62]. For the SACs model, the catalyst surface was simulated using $5 \times 3\sqrt{3} \times 1$ graphene with a vacuum layer of 20 Å [63]. For geometry optimization, rigorous parameters were employed: a 450 eV cutoff energy, coupled with a $2 \times 2 \times 1$ Γ-centered k-point mesh, proved scientifically adequate and ensured convergence (Fig. S1). The force criteria requirements were set to 0.02 eV/Å for each atom. The investigation into the reaction mechanism of SO_2 on the catalytic oxidation of NO by H_2O_2 utilized settings of IBRION= 3 and ISPIN= 2 within the VASP INCAR file [64]. Given the heightened precision demands of electronic configurations and ground state energies, we escalated our computational rigor by adopting a $4 \times 4 \times 1$ k-point grid for electronic self-consistent calculations, along with a tight convergence threshold of 10^{-5} eV [65]. Finally, to delve into charge distribution insights, the Bader charge analysis method was meticulously applied. The calculation equations of binding energy, adsorption energy, energy barrier, and electronegativity were provided in the Supporting information.

3. Results and discussion

3.1. Experiments

To delve into the underlying mechanism in which the influence of SO_2 on the oxidation of NO catalyzed by H_2O_2, we conduct a series of characterizations on the Fe-N_4-C. Extended X-ray absorption fine structure (EXAFS) are conducted to probe the local environment of Fe atoms (Fig. S2). The optimal fitting analysis of the EXAFS spectra for Fe-

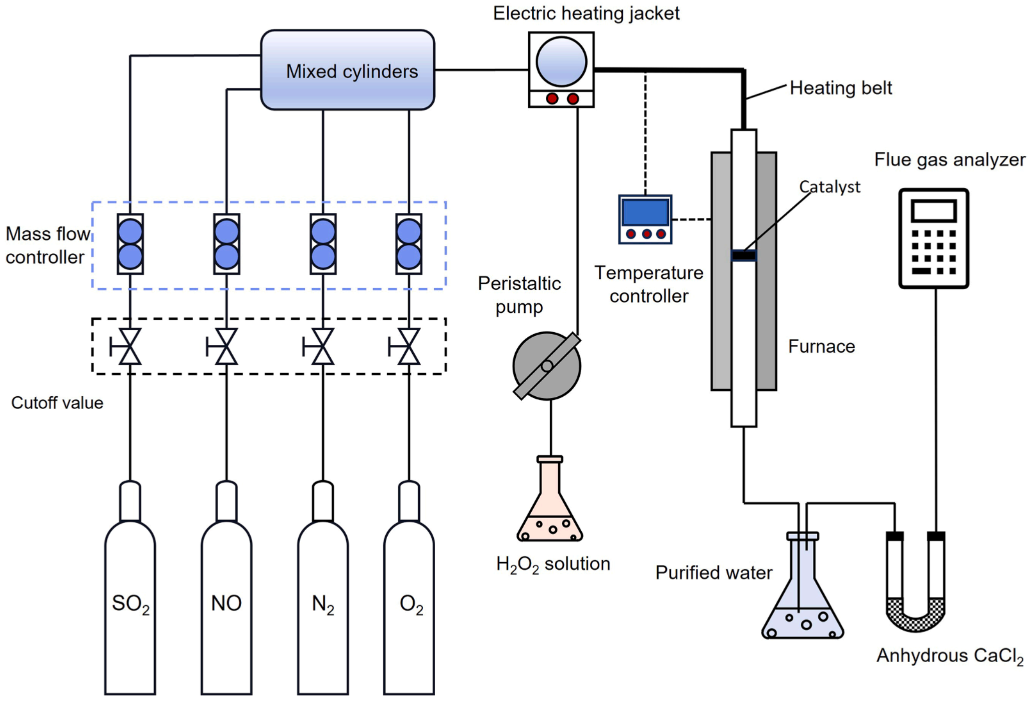

Fig. 2. Schematic diagram of the experimental apparatus.

N_4-C (Fig. 3a) demonstrates that the Fe atom is coordinated with four N atoms, in harmony with DFT calculation. Powder X-ray diffraction (XRD) of Fe-N_4-C exhibited two broad peaks at approximately 26° and 44°, attributable to the (002) and (101) planes of graphitic carbon, respectively (Fig. 3b). No peak characteristic of Fe-based species can be detected, indicating the Fe-based species are well dispersed on the CN supports. Upon conducting pyrolysis at 900 °C under a nitrogen-rich atmosphere, a distinct regular hexagonal morphology is observed within the catalyst via transmission electron microscopy (TEM), definitively confirming the retention of the ZIF-8 structure (Fig. 3c).

Fig. 3d shows the experiment apparatus for H_2O_2 oxidation NO with the presence of SO_2 on Fe-N_4-C. Initially, 500 ppm NO is introduced into the system, followed by the introduction of gaseous H_2O_2 after NO has stabilized. The concentration of NO is reduced to 252 ppm and stabilized in a short time because H_2O_2 is easily activated by Fe-N_4-C to generate different free radicals. Finally, upon the addition of 500 ppm of SO_2, the NO concentration undergoes a further decline, ultimately stabilizing at 166 ppm. The results show that the removal rate of NO increases from 49.6 % to 66.8 %, indicating that SO_2 enhances the oxidation of NO by H_2O_2 on Fe-N_4-C.

3.2. Adsorption behavior

To achieve clarity regarding the adsorption of diverse gas molecules and sulfides, the adsorption energies of various gas molecules and sulfides on Fe-N_4-C are shown in Fig. 4. Upon adsorbed on solid catalysts, gaseous H_2O_2 is activated easily, transforming into intermediate species with potent oxidizing capabilities, including *O (-1.21 eV), *OH (-1.52 eV), and *OOH (-1.79 eV). NO, NO_2, and HNO_2 exhibit strong adsorption energy on Fe-N_4-C, which indicates that nitride adsorption on Fe-N_4-C is very stable. Furthermore, three different adsorption configurations of SO_2 are observed. These are defined as SO_2^a, SO_2^b, and SO_2^c, separately. The adsorption energy (E_{ads}) of $*SO_2^a$ is −0.66 eV, which belongs to the strong chemical adsorption behavior. Compared with $*SO_2^a$, the adsorption energies of $*SO_2^b$ and $*SO_2^c$ are only −0.30 eV and −0.20 eV, which belong to weak physical adsorption. Under gas-solid conditions, *O, *OH, and *OOH can react with SO_2, yielding sulfides such as $*SO_3$, $*SO_4$, $*HSO_3$, and $*HSO_4$ adsorbed on the surface of Fe-N_4-C. It is notable that the adsorption energies of different sulfides vary significantly. For example, the E_{ads} of $*SO_4$ is as high as −3.49 eV, far exceeding the that of $*SO_2$. Moreover, the two adsorption configurations of HSO_3 (HSO_3^a and HSO_3^b) exhibit comparable energies (-2.68 eV and −2.65 eV), which cannot determine the stable adsorption configuration of HSO_3. Although the E_{ads} of gaseous SO_2 and SO_3 on Fe-N_4-C are marginal, the sulfides formed through the reaction of intermediates with SO_2 exhibit substantial adsorption energies on Fe-N_4-C. This suggests that these sulfides are resistant to removal and may occupy active sites, leading to catalyst poisoning, diminished activity, shortened lifespan, and reduce catalytic performance ultimately. Notably, the E_{ads} of H_2SO_4 on Fe-N_4-C is merely −0.15 eV, indicating minimal impact on the occupation of the active sites. This low energy emphasizes the non-interfering nature of H_2SO_4 in the catalytic process.

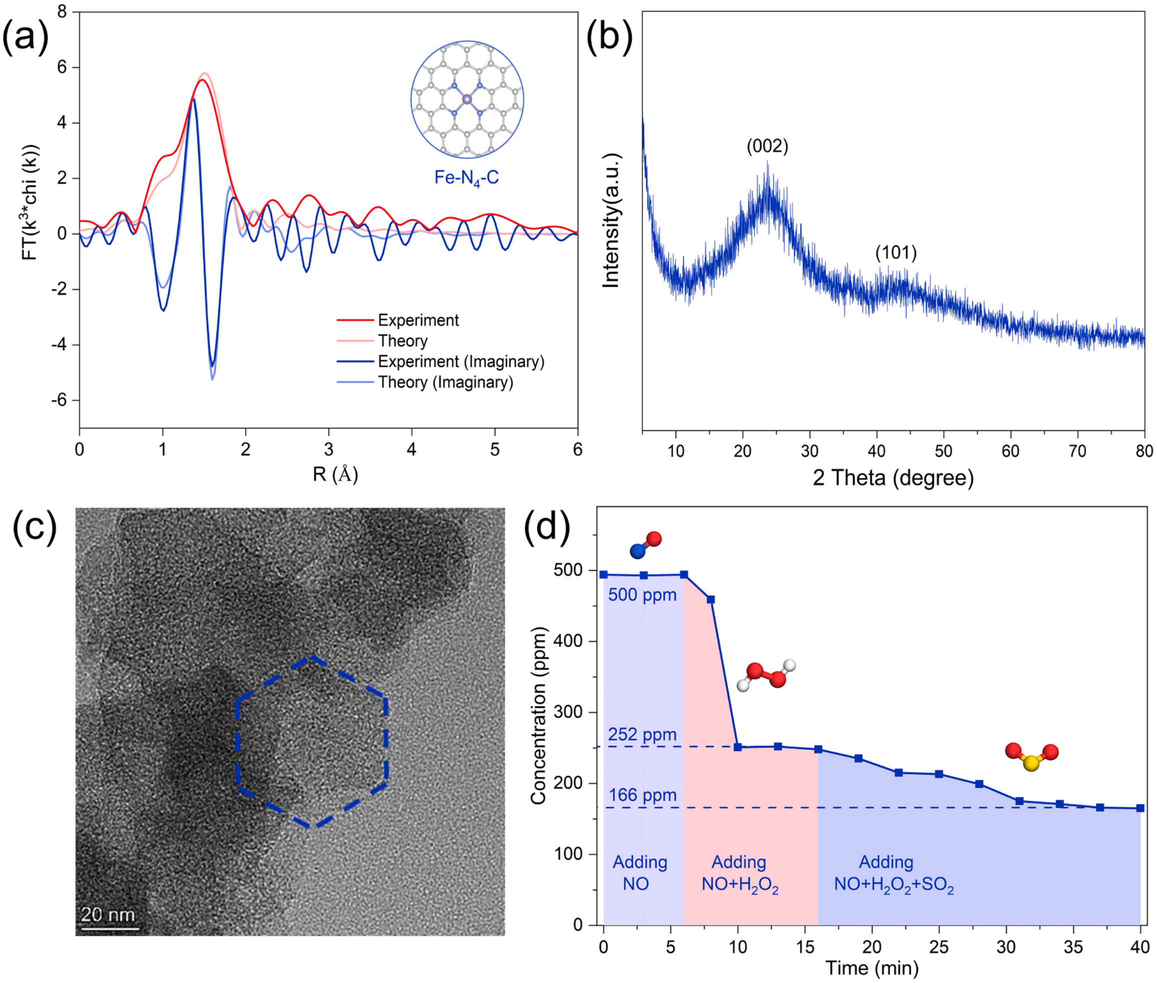

Fig. 3. (a) Fe K-edge EXAFS fitting of Fe-N_4-C. (b) XRD patterns of Fe-N_4-C. (c) Transmission electron microscope of Fe-N_4-C. (d) SO_2 promotion H_2O_2 oxidation NO on Fe-N_4-C. 500 ppm NO concentration, 500 ppm SO_2 concentration, 140 ℃ experiment temperature, 2 mol/L H_2O_2.

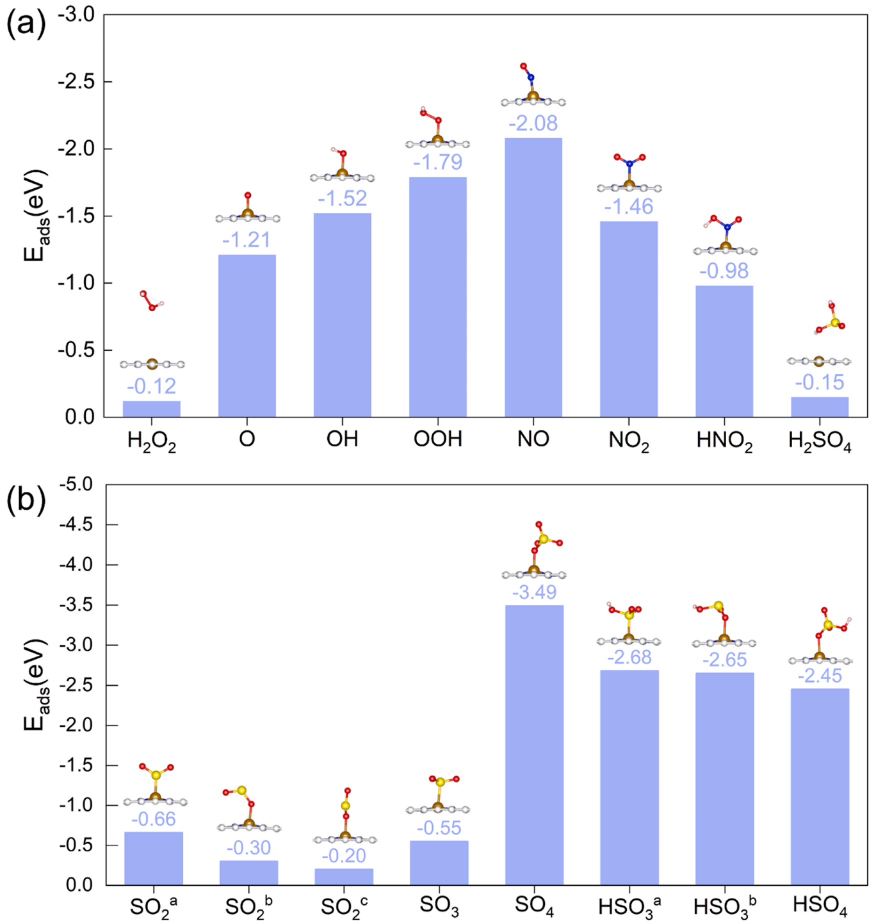

Fig. 4. (a) and (b) Optimized adsorption configurations and energies of gas molecules and sulfides on the Fe-N_4-C.

3.3. SO_2 affection the activation of H_2O_2

The experiments have demonstrated that the presence of SO_2 can promote the activation of H_2O_2 to oxidize NO on Fe-N_4-C. The oxidation of NO using H_2O_2 includes two steps: H_2O_2 is activated into free radicals with strong oxidizing capacity, and these free radicals oxidize NO. However, the precise mechanism by which SO_2 contributes to either enhancing H_2O_2 activation or facilitating NO oxidation remains unclear. The gaseous H_2O_2 adsorbed on Fe-N_4-C activates into three free radicals: O•, •OH, and HO_2•. Among them, the reaction process of H_2O_2 activation into *O and H_2O group is no energy barrier, and the activation energy barrier of *OH and *OOH are 0.09 eV and 1.40 eV. Regarding the interaction between gaseous H_2O_2 and SO_2, the precise reaction pathway remains unknown. Therefore, we selected two potential

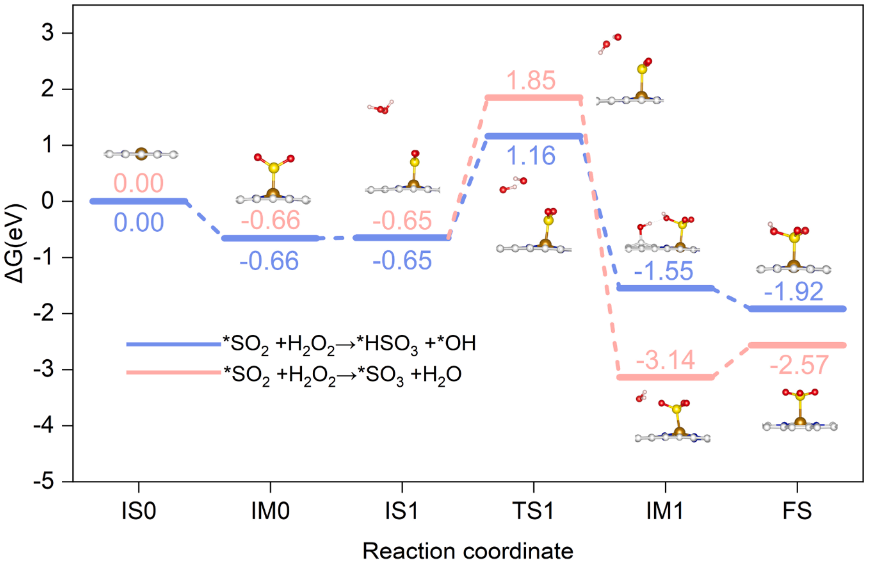

Fig. 5. The reaction pathway of H_2O_2 activation with SO_2. White, blue, brown, red, yellow, and pink spheres represent C, N, Fe, O, S, and H, respectively.

reaction pathways to discuss that how SO_2 affects H_2O_2 activation.

As shown in Fig. 5, the process initiates with the adsorption of SO_2 at the Fe site. The adsorption structure of SO_2 is more stable than that of H_2O_2 because the E_{ads} of SO_2 is greater than that of H_2O_2 (-0.12 eV). Subsequently, gaseous H_2O_2 enters the reaction environment, its inherent instability leads to two potential reaction pathways. One pathway is that the O-O bond in H_2O_2 is broken and two •OH radicals appear on the surface of the catalyst when H_2O_2 is close to SO_2. One •OH is absorbed on the carbon, while the other forms an S-OH bond with the adsorbed SO_2, ultimately transforming into *HSO_3 adsorbed at the Fe site. The energy barrier (E_b) of this reaction process is 2.5 eV. Another pathway involves SO_2 attacking the O atoms in H_2O_2, resulting in the formation of *SO_3 and H_2O. The H_2O molecule directly escapes into the vacuum layer without adsorbing on the catalyst surface. This pathway has an E_b of 1.81 eV. The complete reaction processes are shown in Fig. S3. Obviously, the energy barrier for the reaction between SO_2 and H_2O_2 (1.81 eV) is considerably larger than the activation energy barrier of H_2O_2. Higher energy barriers correspond to slower the reaction rate. It means that the presence of SO_2 has little effect on the activation of H_2O_2 in a low-temperature environment.

3.4. The reaction path of sulfides oxidation of NO

Reaction energy barriers of SO_2 and H_2O_2 shows that SO_2 does not improve the activation of H_2O_2 on Fe-N_4-C, thus supporting the hypothesis that SO_2 may enhance NO oxidation. SO_2 itself cannot react directly with NO, so this promotion is caused by sulfides produced by SO_2 interacting with intermediate free radicals. However, some sulfides possessing heightened adsorption energies may occupy active sites of the catalyst and lack the ability to desorb, thereby hindering catalytic processes. Fig. 6 illustrates 8 various pathways involving SO_2 and NO, and we will delve into the atomic transformations, along with their respective reaction energy barriers in the subsequent discussion.

3.4.1. Reaction pathways of NO oxidation by *HSO_3

*HSO_3 is formed by the interaction between *OH and SO_2. Two distinct adsorption configurations (*HSO_3^a and *HSO_3^b) are absorbed on the Fe site of the catalyst (Fig. S4). Although the adsorption energies of both configurations are comparable (-2.68 eV and −2.65 eV, respectively), there are notable variations in the bond lengths between the Fe atom and the adsorbed species. In the *HSO_3^a configuration, the S atom of *HSO_3 is securely anchored at the Fe site of the Fe-N_4-C, forming a Fe-S bond of 2.16 Å and an OH-S bond of 1.68 Å. Conversely, in the *HSO_3^b configuration, the O atom of *HSO_3 assumes the position at the Fe site, resulting in a Fe-O bond length of 1.95 Å and a slight elongation of the OH-S bond to 1.71 Å. These differences in adsorption configurations are striking and highlight the unique structural features of each HSO_3 species. Both configurations possess the potential to catalyze the oxidation of NO, but their distinct molecular arrangements suggest varying degrees of efficacy in this process. In the subsequent sections, we will delve into the oxidation effects of these two *HSO_3 configurations, exploring how their unique adsorption patterns contribute to their catalytic performance.

Next, we embark on an analysis of the reaction pathways for the oxidation of NO by *HSO_3. As illustrated in Fig. 7a, the process initiates with the adsorption of *OH which is generated through H_2O_2 activation at the Fe site. Subsequently, SO_2 enters the system and reacts with the adsorbed *OH. This reaction is marked by the gradual weakening of the Fe-O bond and the concurrent formation of a Fe-S bond, ultimately resulting in the adsorption of *HSO_3^a on the Fe-N_4-C. This process has an E_b of 0.87 eV. Path 1 and Path 2 represent the process by which *HSO_3^a oxidizes NO and NO_2. In Path 1, NO actively attacks *HSO_3^a, resulting in the rupture of the OH-S bond and the formation of HNO_2, which subsequently desorbs into the vacuum layer. This process has an E_b of 0.59 eV. In Path 2, NO_2 targets the OH moiety of *HSO_3^a, yielding HNO_3 that detaches from the catalyst surface. The E_b of this process is 0.89 eV. After the production of HNO_2 and HNO_3, only *SO_2^a remains adsorbed on the catalyst. The adsorption energy of *SO_2^a on Fe-N_4-C is low (-0.66 eV), facilitating its easy desorption and minimizing the blockage of active sites. The complete reaction processes are shown in Fig. S5–7 . From an energetic perspective, the E_b of NO oxidation by *HSO_3^a (0.59 eV) is lower than that for NO_2 oxidation by *HSO_3^a (0.89 eV), suggesting that *HSO_3^a favors the oxidation of NO over NO_2. Within the overall reaction sequence, the formation of *HSO_3^a from SO_2 and *OH, with an E_b of 0.87 eV, emerges as the rate-limiting step.

The remarkable ability of *HSO_3^a to oxidize NO prompts our speculation that *HSO_3^b may similarly exhibit such a capacity (Path 3 and 4). As shown in Fig. 7b, the formation mechanism of *HSO_3^b parallels that of *HSO_3^a, where *OH adsorbs onto the Fe site of Fe-N_4-C, followed by the intrusion of SO_2 to attack the *OH, leading to the rupture of the Fe-O bond. Notably, in *HSO_3^b, the O atom from SO_2 forms a bond with the Fe atom, ultimately establishing the Fe-O bond, which differs from the generation of *HSO_3^a. The E_b of this process is 0.58 eV, which is 0.29 eV lower than that observed in the formation of *HSO_3^a. *HSO_3^a and *HSO_3^b share a commonality in oxidizing NO and NO_2; both processes involve the abstraction of OH from *HSO_3 to yield HNO_2 and HNO_3. However, the energy barrier values diverge significantly. The E_b of NO oxidation by *HSO_3^b is only 0.37 eV, and that of NO_2 oxidation is as high as

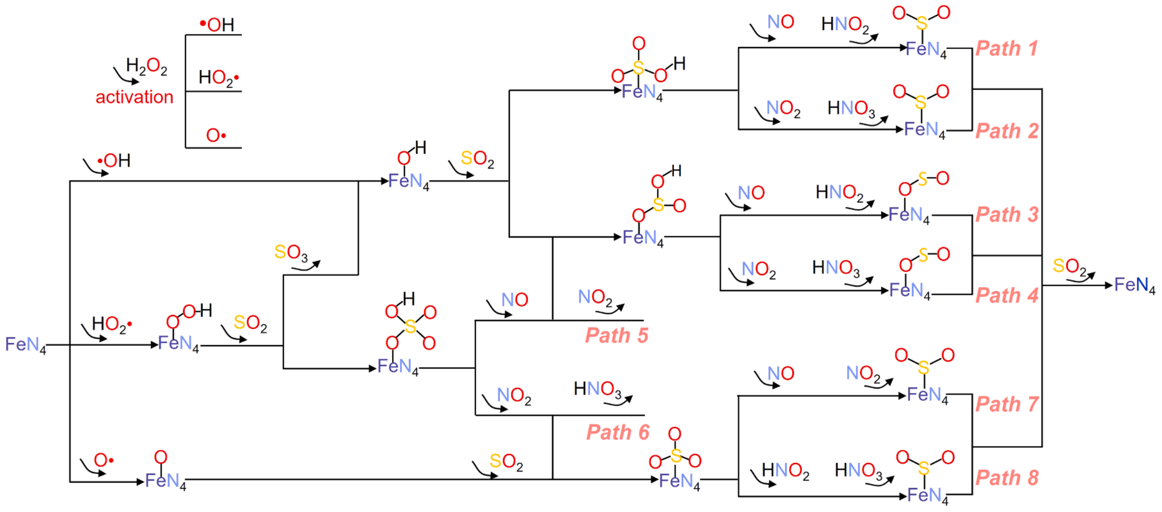

Fig. 6. Proposed reaction network of SO_2 involved in the oxidation of NO by H_2O_2. (Path 1–8).

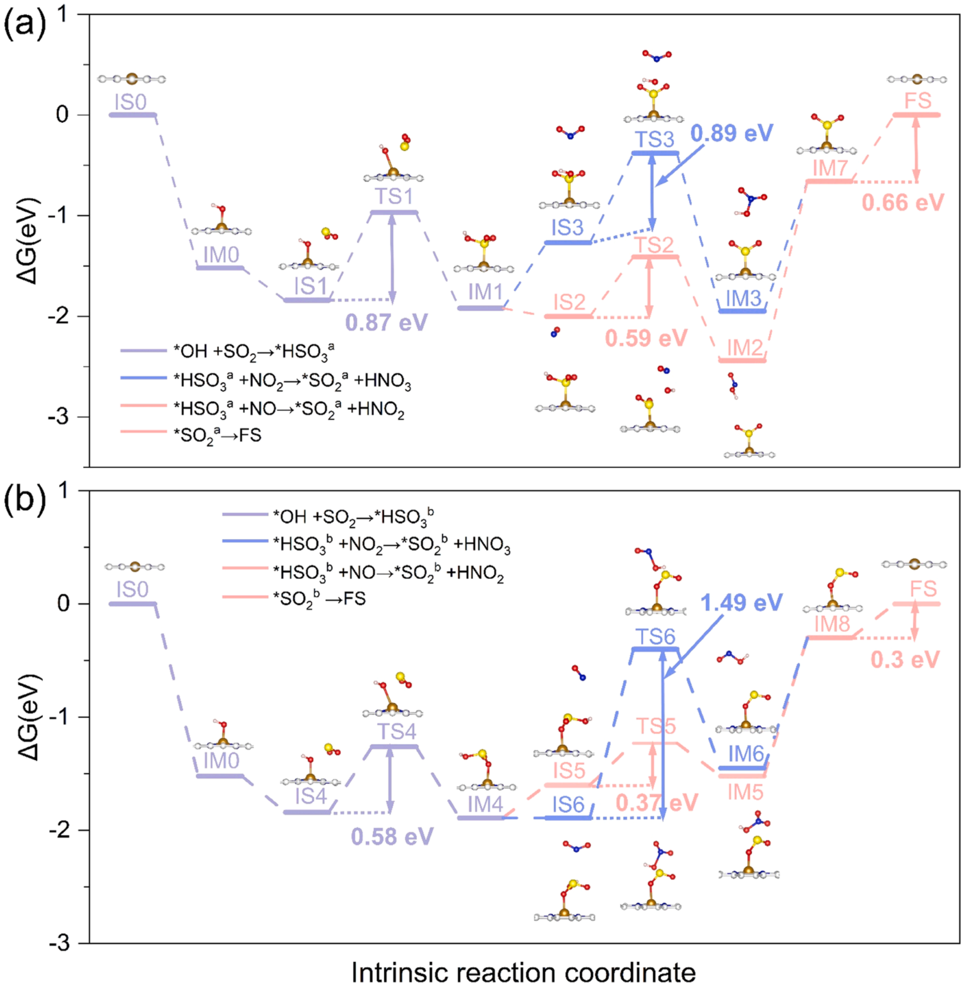

Fig. 7. The reaction pathway of NO oxidation by *OH and SO_2. (a) The reaction pathways for the generation of $*HSO_3^a$ and oxidation of nitrides. (Path 1 and 2) (b) The reaction pathways for the generation of $*HSO_3^b$ and oxidation of nitrides. (Path 3 and 4) White, blue, brown, red, yellow, and pink spheres represent C, N, Fe, O, S, and H, respectively.

1.49 eV. Consequently, $*HSO_3^b$ emerges as a more potent oxidant for NO, while $*HSO_3^a$ is more effective in NO_2 oxidation. Moreover, the adsorption configuration of $*SO_2$ subsequent to NO oxidation by $*HSO_3^b$ differs distinctly from that observed during NO oxidation by $*HSO_3^a$. The desorption energy of $*SO_2^b$ is markedly lower, at 0.3 eV, which is a reduction of 0.36 eV compared to $*SO_2^a$. Throughout the entire reaction sequence, the efficacy of $*HSO_3^b$ in NO oxidation surpasses that of $*HSO_3^a$, with a maximum E_b of merely 0.58 eV. The complete reaction processes are shown in Fig. S8–10. The parallel reaction pathways of NO oxidation catalyzed by $*HSO_3^a$ and $*HSO_3^b$ serve as compelling evidence that SO_2 acts as a facilitator, enhancing the oxidation of NO by *OH.

3.4.2. *Reaction pathways of NO oxidation by $*HSO_4$*

HO_2•, akin to •OH, is an important free radical in the activation process of H_2O_2. Its adsorption onto Fe-N_4-C exhibits a robust chemical binding characterized by an adsorption energy of −1.75 eV. *OOH and SO_2 engage in two distinct reaction pathways. As illustrated in Fig. S11, in one pathway, SO_2 efficiently strips the O atom from *OOH, resulting in the formation of SO_3, which promptly desorbs from the catalyst surface in gaseous form. Meanwhile, the leftover *OH remains adsorbed on the catalyst surface. This reaction pathway has an energy barrier of 0.4 eV and is exothermic in nature, signifying its thermodynamic favorability. The conversion of *OOH to *OH indicates that the relationship between adsorbed substances is also complex and changeable.

As shown in Fig. 8a, an alternative pathway involves SO_2 attacking the O-O bond of *OOH, ultimately leading to the adsorption of $*HSO_4$ on the Fe-N_4-C surface. This process encounters an energy barrier of 0.75 eV. $*HSO_4$ also possesses the capacity to oxidize both NO and NO_2. (Path 5 and 6) When NO_2 engages in the reaction, it targets the OH of $*HSO_4$, triggering the formation of HNO_3. This process has an energy barrier of 1.18 eV. Because the OH of $*HSO_4$ is seized by NO_2, the O-S bond in $*HSO_4$ is severed, diminishing the van der Waals force between the O and S atoms. The stable $*SO_3$ adsorption configuration cannot be directly formed on the catalyst, but *O and SO_2 are formed which continue to react. This reaction involves the rupture of Fe-O bonds and the formation of Fe-S bonds, culminating in the adsorption of $*SO_3$ on the catalyst surface. This process has an E_b of 0.58 eV, and the desorption energy of $*SO_3$ is 0.55 eV, indicating that it is easily desorption. ensuring that the active site remains unoccupied throughout the reaction cycle, thereby facilitating its recycling. In the case of $*HSO_4$ oxidizing NO, the NO abstracts an O atom from $*HSO_4$, causing the S-O bond to fracture and the formation of NO_2. $*HSO_4$ is converted into $*HSO_3^b$ adsorbed on Fe-N_4-C. This step is hindered by an energy barrier of 1.71 eV. The complete reaction processes are shown in Fig. S12–14. As the oxidation of NO by HSO_3 has been previously elaborated upon in the article, we refrain from repeating the details here.

When focusing on the oxidation of NO by *OOH, the energy barrier (E_b) for this reaction is merely 0.14 eV. Conversely, the E_b for the oxidation of both NO and NO_2 by $*HSO_4$ significantly surpasses 0.14 eV, indicating that SO_2 does not enhance the efficiency of NO oxidation by

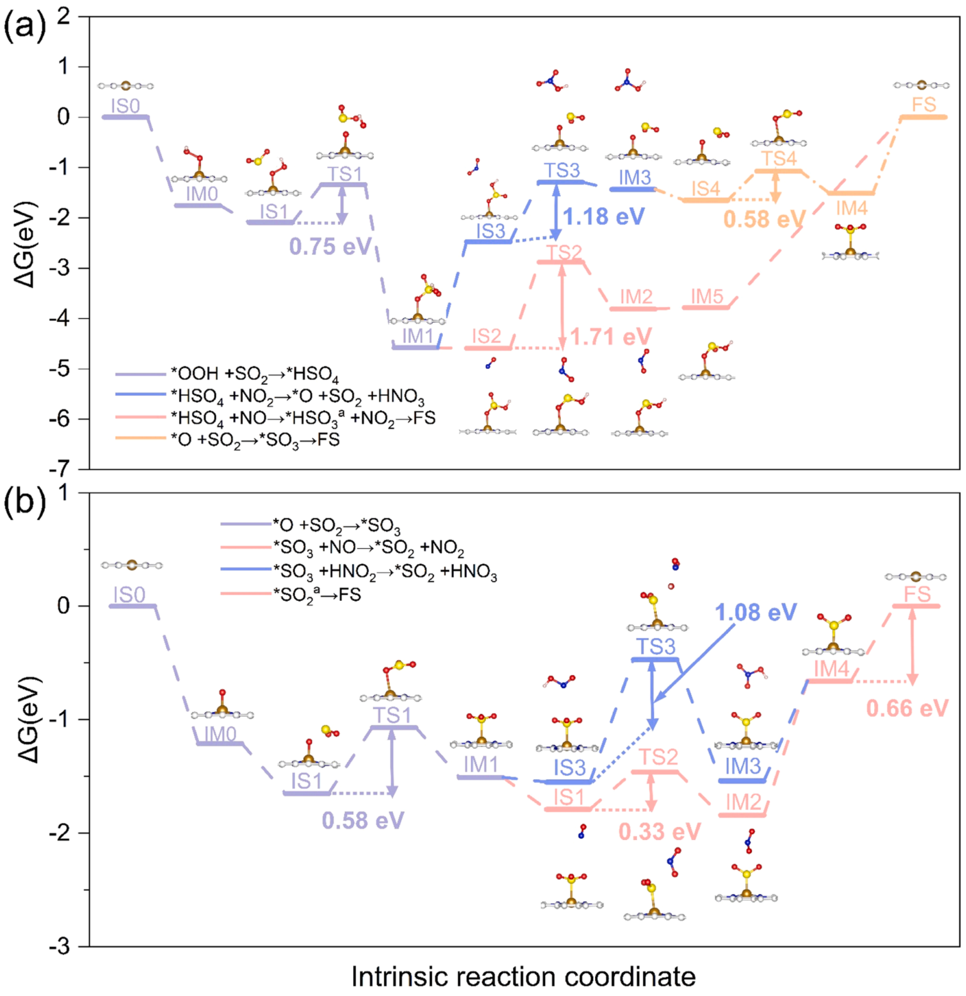

Fig. 8. (a) The reaction pathway of NO oxidation by *OOH and SO_2. (Path 5 and 6) (b) The reaction pathway of NO oxidation by *O and SO_2. (Path 7 and 8) White, blue, brown, red, yellow, and pink spheres represent C, N, Fe, O, S, and H, respectively.

*OOH. However, the substantial energy barrier required for activation H_2O_2 into *OOH may hinder the abundant generation of *OOH on Fe-N_4-C surfaces, thereby limiting its oxidative capacity. Furthermore, the mechanisms governing how SO_2 influences the oxidation of NO by other intermediates remain elusive and need further investigation.

3.4.3. *Reaction pathways of NO oxidation by *SO_3*

Finally, we delve into NO oxidation by SO_3. Because there is no energy barrier for H_2O_2 to be activated to *O on Fe-N_4-C, a large amount of *O exist on the surface of the catalyst. As illustrated in Fig. 8b, the formation of *SO_3 from the reaction between SO_2 and *O boasts a relatively low energy barrier of 0.58 eV, and the facile desorption of *SO_3 subsequently frees up numerous active sites for further oxidation. Moreover, *SO_3 also possesses the capability to oxidize NO. Two distinct reaction pathways are proposed (Path 7 and 8). Path 7 shows that NO directly attacks the O atom of *SO_3, resulting in the cleavage of the S-O bond and the release of gaseous NO_2, leaving behind an adsorbed *SO_2^a configuration on Fe-N_4-C. This reaction pathway has an energy barrier of 0.33 eV. Path 8 involves the oxidation of HNO_2, where HNO_2 captures an O atom from *SO_3. Prior to this, the O-H bond in HNO_2 is ruptured, enabling the free H atom to form a new O-H bond with the O atom on *SO_3. Concurrently, the S-O bond breaks and combines with NO_2 to yield HNO_3. This process has a higher energy barrier of 1.08 eV. The complete reaction processes are shown in Fig. S15–17. Upon completion of Path 8, only SO_2 remains adsorbed on Fe-N_4-C in the form of *SO_2^a, with a desorption energy of 0.66 eV, which is conducive to catalyst recycling and reuse. Imaginary frequency statistics of different transition state reaction processes in the NO oxidation by sulfides are shown in Table S2.

Some free radicals can react with SO_2 to form *SO_4. Based on this, we begin to discuss the reaction process for the oxidation of NO by *SO_4 on Fe-N_4-C. As shown in Fig. S18, NO targets the O atom of *SO_4, fostering the formation of an N-O bond while the S-O bond cleavages, ultimately yielding NO_2. As in the case of NO oxidation by *HSO_4, SO_3 fails to stabilize in a Fe-O bond configuration on Fe-N_4-C, leading to the surface being left with only *O and free SO_2. Notably, this reaction is endothermic, featuring an energy barrier of 0.94 eV, which is higher than E_b of *HSO_3 for the oxidation of NO. The electron transfer from the catalyst to *SO_4 is 1.32 eV during the reaction process. This less favorable reaction pathway is unlikely to enhance the catalytic oxidation of NO by H_2O_2.

3.5. *Energy barriers of rate-determination step*

The activation process of H_2O_2 is an important part of the whole reaction. However, the substantial reaction energy barrier between H_2O_2 and SO_2 implies that SO_2 faces challenges in influencing the activation of H_2O_2. Our discussion will delve into the reaction mechanism of SO_2 to promote NO oxidation.

Fig. 9a illustrates the reaction of NO oxidation by *OH on Fe-N_4-C with and without SO_2. Although the E_b of NO oxidation by *OH is small (0.21 eV), the RDS (Rate-Determination Step) energy barrier of the

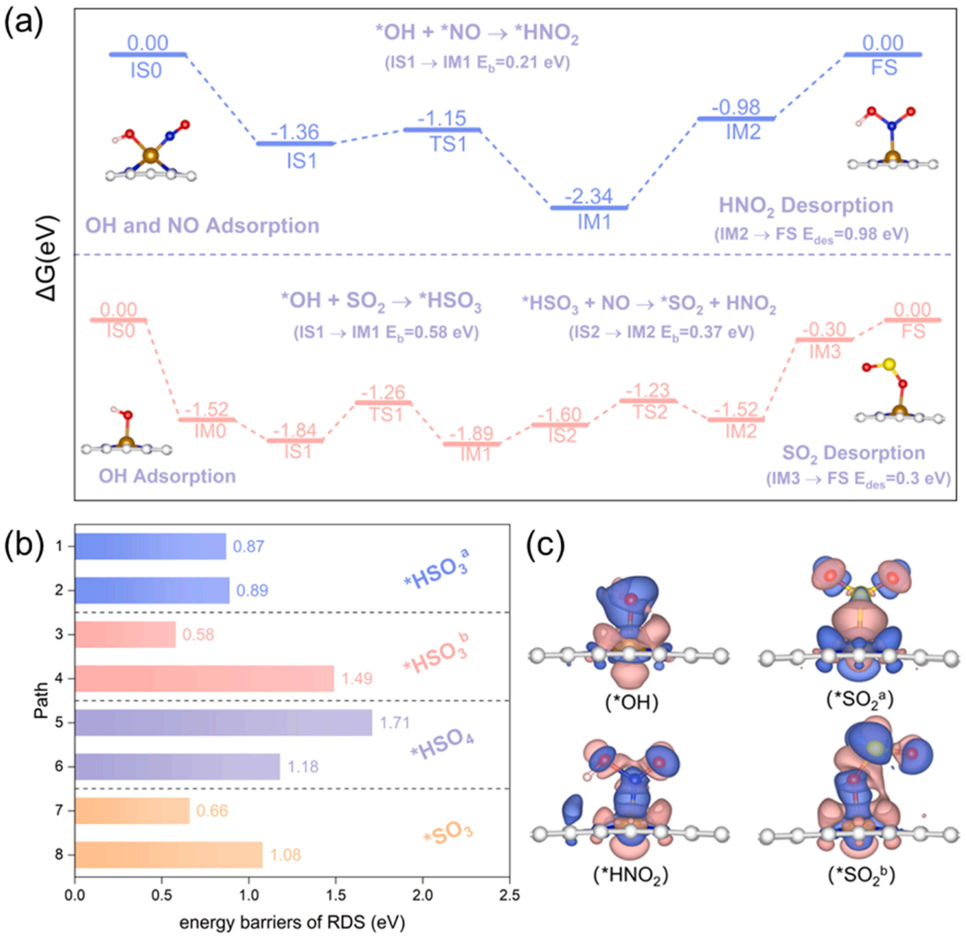

Fig. 9. (a) The rate-determination step (RDS) reaction processes of NO oxidation by *OH with and without SO_2. (b) The RDS energy barriers of different pathways. (b) Calculated charge density differences induced by sulfide adsorption on Fe-N_4-C. Contour lines in the plots are drawn at 0.001 e Å^{-3} intervals. Blue and red areas represent electron gain and loss, respectively. White, blue, brown, red, yellow, and pink spheres represent C, N, Fe, O, S, and H, respectively.

whole reaction process is the desorption energy of HNO_2 (0.98 eV) [66]. The complete reaction processes are shown in Fig. S19. This means that HNO_2 is difficult to desorb from Fe-N_4-C and occupies the active site of the catalyst, which is extremely detrimental to the whole reaction process. When SO_2 participates in the oxidation of NO by *OH, the RDS of the whole reaction process is: $*SO_2 + OH \rightarrow *HSO_3^b$, and the energy barrier is 0.58 eV. In addition, after the oxidation of NO to HNO_2 is completed, only $*SO_2^b$ with a desorption energy of 0.3 eV is adsorbed on Fe-N_4-C. Therefore, the presence of SO_2 changes the mode of desorption, which greatly reduces the energy barrier of the rate-determining step. Fig. 9**b** illustrates the energy barriers of rate-determination step (RDS) in the oxidation of various nitrides via distinct reaction pathways. The minimal energy barrier of RDS involving $*HSO_3^b$ stands at a mere 0.58 eV. This means that $*HSO_3^b$ has the strongest oxidation energy for nitride during the whole removal process (Path 3). Notably, the energy barriers above are significantly lower than those of the previously studied metal−organic framework, zeolites, and spinel catalysts with various potential oxidants, as summarized in Table S3.

Furthermore, we conduct an EDD (electron density difference) analysis (Fig. 9**c**) The gas molecules are mainly surrounded by the blue color, indicating that the gas gains electron during adsorption. Conversely, the presence of red region around the metal atoms demonstrates that Fe acts as the donor to transfer electrons to the gas molecules. As shown in Table S4, we delve into the charge transfer (*Q*) incurred by *OH, $*SO_2^a$, $*SO_2^b$, and $*HNO_2$ upon desorption and the bond length (*d*) between the metal atom and the gas molecules. The desorption of $*SO_2^a$ has the smallest charge transfer (-0.93 eV) and the largest bond length (2.01 Å). The strong positive correlation emerges between the desorption energy and charge transfer among the adsorbed substances, offering an electron transfer-based explanation for the disparities in desorption energies among different species.

4. Conclusion

In summary, the mechanism underlying the promotion of SO_2 on the oxidation of NO by H_2O_2 is elucidated. Initially, experiments involving the Fe-N_4-C catalyst for the oxidation of NO by H_2O_2 demonstrate that SO_2 enhances the removal of NO. Subsequently, Density Functional Theory (DFT) calculations are employed to determine the adsorption energies of various sulfides on Fe-N_4-C. Notably, SO_2 exhibits a low adsorption energy on the catalyst, whereas certain sulfides exhibit significantly higher adsorption energies. Ultimately, the promotional effect of SO_2 is analyzed from the perspectives of H_2O_2 activation and NO oxidation, leading to the identification of eight oxidation pathways. Among these, the path involving $*HSO_3^b$ oxidizing NO has the lowest reaction energy barrier of only 0.58 eV. We anticipate that our findings will provide fresh theoretical insights for NO removal strategies. which provide a new way for the removal of NO. We hope that our conclusions can provide a new theoretical guidance for NO removal.

CRediT authorship contribution statement

Yixiao Sun: Writing – original draft, Methodology, Formal analysis, Data curation. **Zhengyang Gao:** Writing – original draft, Software, Methodology, Funding acquisition, Formal analysis, Conceptualization. **Ziwei Miao:** Visualization, Investigation. **Xiang Li:** Supervision, Resources. **Yuanzheng Qu:** Writing – original draft, Validation. **Weijie Yang:** Writing – review & editing, Supervision, Resources, Funding acquisition, Conceptualization. **Shilong Chen:** Validation, Software.

Declaration of Competing Interest

The authors declare that they have no known competing financial interests or personal relationships that could have appeared to influence the work reported in this paper.

Acknowledgement

This work was funded by the National Natural Science Foundation of China (Nos. 52176104 and 52006073).

Appendix A. Supporting information

Supplementary data associated with this article can be found in the online version at doi:10.1016/j.jece.2025.115439.

Data availability

Data will be made available on request.

References

[1] Q.-J. Fang, J.-k Pan, W. Zhang, F.-l Sun, W.-x Chen, Y.-f Yu, A.-F. Hu, G.-l Zhuang, Cooperatively interface role of surface atoms and aqueous media on single atom catalytic property for H_2O_2 synthesis, J. Colloid Interface Sci. 617 (2022) 752–763, https://doi.org/10.1016/j.jcis.2022.03.052.

[2] Z. Fan, G. Cheng, J. Liu, Y. Su, C. Feng, X. Wu, Insight into the temperature-dependent SO_2 resistance over Mn-based de-NO_x catalyst, J. Environ. Chem. Eng. 11 (3) (2023) 110202, https://doi.org/10.1016/j.jece.2023.110202.

[3] Z. Song, B. Wang, J. Yu, C. Ma, T. Chen, W. Yang, S. Liu, L. Sun, Effect of Ti doping on heterogeneous oxidation of NO over Fe_3O_4 (1 1 1) surface by H2O2: a density functional study, Chem. Eng. J. 354 (2018) 517–524, https://doi.org/10.1016/j.cej.2018.08.042.

[4] H. Fu, J. Wei, G. Chen, M. Xu, J. Liu, J. Zhang, K. Li, Q. Xu, Y. Zou, W.-x Zhang, S. Xi, X. Chen, S. Li, L. Ling, Axial coordination tuning Fe single-atom catalysts for boosting H_2O_2 activation, Appl. Catal. B: Environ. 321 (2023) 122012, https://doi.org/10.1016/j.apcatb.2022.122012.

[5] J. Ding, Q. Zhong, H. Cai, S. Zhang, Structural characterizations of fluoride doped CeTi nanoparticles and its differently promotional mechanisms on ozonation for low-temperature removal of NO_x ($x = 1, 2$), Chem. Eng. J. 286 (2016) 549–559, https://doi.org/10.1016/j.cej.2015.10.055.

[6] Y. Li, H. Yi, X. Tang, X. Liu, Y. Wang, B. Cui, S. Zhao, Study on the performance of simultaneous desulfurization and denitrification of Fe_3O_4-TiO_2 composites, Chem. Eng. J. 304 (2016) 89–97, https://doi.org/10.1016/j.cej.2016.06.035.

[7] B. Wu, Y. Xiong, A novel low-temperature NO removal approach with •OH from catalytic decomposition of H_2O_2 over $La_{1-x}Ca_xFeO_3$ oxides, J. Chem. Technol. Biotechnol. 93 (1) (2017) 43–53, https://doi.org/10.1002/jctb.5317.

[8] Y. Zhao, B. Yuan, R. Hao, Z. Tao, Low-temperature conversion of NO in flue gas by vaporized H_2O_2 and nanoscale zerovalent iron, Energy Fuels 31 (7) (2017) 7282–7289, https://doi.org/10.1021/acs.energyfuels.7b00588.

[9] R. Cui, S. Ma, J. Wang, S. Sun, NO oxidation over Fe-based catalysts supported on montmorillonite K10, gamma-alumina and ZSM-5 with gas-phase H_2O_2, Chemosphere 234 (2019) 302–309, https://doi.org/10.1016/j.chemosphere.2019.06.029.

[10] F. Gao, Y. Niu, Y. Cui, Y. Liu, N. Luo, J. Wen, E. Duan, C. Wang, H. Yi, Y. Zhou, X. Tang, Excellent performance of Ce doped $CoMn_2O_4/TiO_2$ catalyst in NH3-SCR of NO under H_2O&SO_2 conditions, J. Environ. Chem. Eng. 12 (5) (2024) 113849, https://doi.org/10.1016/j.jece.2024.113849.

[11] M. Liu, Q. Wang, Y. Zhao, B. Zhao, H. Li, T. Sun, Enhanced activity and SO_2 tolerance in low-temperature NH_3-SCR of NOx over MnCr catalyst by hetero-oxide modification, J. Environ. Chem. Eng. 11 (6) (2023) 111508, https://doi.org/10.1016/j.jece.2023.111508.

[12] J. Ding, Q. Zhong, S. Zhang, Simultaneous removal of NO_X and SO_2 with H_2O_2 over Fe based catalysts at low temperature, RSC Adv. 4 (11) (2014) 5394–5398, https://doi.org/10.1039/c3ra46418k.

[13] Z. Song, B. Wang, W. Yang, T. Chen, W. Li, C. Ma, L. Sun, Research on NO and SO2 removal using TiO2-supported iron catalyst with vaporized H_2O_2 in a catalytic oxidation combined with absorption process, Environ. Sci. Pollut. Res Int 27 (15) (2020) 18329–18344, https://doi.org/10.1007/s11356-020-08042-6.

[14] H. Luo, J. Wang, C. Wang, Z. Luo, L. Qu, Decomplexation of Cu(II)-EDTA by heat assisted CuO catalyzed H_2O_2: sequential addition of H2O2, kinetics, mechanism and catalyst reutilization, J. Environ. Chem. Eng. 12 (3) (2024) 112800, https://doi.org/10.1016/j.jece.2024.112800.

[15] L. Zhang, S. Jiang, Y. Jia, M. Zhang, J. Guo, Effects of Na^+/H_2O_2 on nitrogen removal and sludge activity: Performance and mechanism, J. Environ. Chem. Eng. 12 (5) (2024) 113194, https://doi.org/10.1016/j.jece.2024.113194.

[16] R. Hao, Y. Zhao, B. Yuan, S. Zhou, S. Yang, Establishment of a novel advanced oxidation process for economical and effective removal of SO_2 and NO, J. Hazard. Mater. 318 (2016) 224–232, https://doi.org/10.1016/j.jhazmat.2016.06.052.

[17] X. Liu, Ca Wang, T. Zhu, Q. Lv, Y. Li, D. Che, Simultaneous removal of NO and SO_2 from coal-fired flue gas based on the catalytic decomposition of H_2O_2 over $Fe_2(MoO_4)_3$, Chem. Eng. J. 371 (2019) 486–499, https://doi.org/10.1016/j.cej.2019.04.028.

[18] Y. Zhao, T.-X. Guo, Z.-Y. Chen, Y.-R. Du, Simultaneous removal of SO_2 and NO using M/$NaClO_2$ complex absorbent, Chem. Eng. J. 160 (1) (2010) 42–47, https://doi.org/10.1016/j.cej.2010.02.060.

[19] J. Ding, Q. Zhong, S. Zhang, F. Song, Y. Bu, Simultaneous removal of NO_X and SO_2 from coal-fired flue gas by catalytic oxidation-removal process with H_2O_2, Chem. Eng. J. 243 (2014) 176–182, https://doi.org/10.1016/j.cej.2013.12.101.

[20] B. Wu, Y. Xiong, Y. Ge, Simultaneous removal of SO_2 and NO from flue gas with OH from the catalytic decomposition of gas-phase H_2O_2 over solid-phase $Fe_2(SO_4)_3$, Chem. Eng. J. 331 (2018) 343–354, https://doi.org/10.1016/j.cej.2017.08.097.

[21] S. Jia, G. Pu, J. Gao, C. Yuan, Oxidation-absorption process for simultaneous removal of NO_x and SO_2 over Fe/Al2O3@SiO_2 using vaporized H_2O_2, Chemosphere 291 (2022) 133047, https://doi.org/10.1016/j.chemosphere.2021.133047.

[22] Y. Zhao, B. Yuan, Y. Shen, R. Hao, S. Yang, Simultaneous removal of NO and SO_2 from flue gas using vaporized H_2O_2 catalyzed by nanoscale zero-valent iron, Environ. Sci. Pollut. Res Int 25 (25) (2018) 25526–25537, https://doi.org/10.1007/s11356-018-2628-4.

[23] L. Chen, W. Yang, Y. Wang, Z. Liang, Q. Zhao, Q. Lu, Investigation on the NO removal from simulated flue gas by using H_2O_2 vapor over $Fe_2(MoO_4)_3$, Energy Fuels 32 (8) (2018) 8605–8613, https://doi.org/10.1021/acs.energyfuels.8b01487.

[24] B. Yang, S. Ma, R. Cui, J. Wang, S. Sun, S. Li, Novel low-cost simultaneous removal of NO and SO_2 with ·OH from decomposition of H_2O_2 catalyzed by alkali-magnetic modified fly ash, Ind. Eng. Chem. Res. 58 (13) (2019) 5339–5347, https://doi.org/10.1021/acs.iecr.9b01014.

[25] Z. Song, B. Wang, W. Yang, T. Chen, C. Ma, L. Sun, Simultaneous removal of NO and SO_2 through heterogeneous catalytic oxidation-absorption process using magnetic $Fe_{2.5}M_{0.5}O_4$ (M = Fe, Mn, Ti and Cu) catalysts with vaporized H_2O_2, Chem. Eng. J. 386 (2020) 123883, https://doi.org/10.1016/j.cej.2019.123883.

[26] R. Cui, S. Ma, B. Yang, S. Li, T. Pei, J. Li, J. Wang, S. Sun, C. Mi, Simultaneous removal of NO_x and SO_2 with H_2O_2 over silica sulfuric acid catalyst synthesized from fly ash, Waste Manag 109 (2020) 65–74, https://doi.org/10.1016/j.wasman.2020.04.049.

[27] S. Jia, G. Pu, W. Xiong, P. Wang, J. Gao, C. Yuan, Investigation on simultaneous removal of SO_2 and NO over a Cu–Fe/TiO_2 catalyst using vaporized H_2O_2: an analysis on SO_2 effect, Ind. Eng. Chem. Res. 60 (37) (2021) 13474–13484, https://doi.org/10.1021/acs.iecr.1c01012.

[28] Y. Tang, W. Chen, J. Zhou, H. Chai, Y. Li, Y. Cui, Z. Feng, X. Dai, Mechanistic insight into the selective catalytic oxidation for NO and CO on co-doping graphene sheet: a theoretical study, Fuel 253 (2019) 1531–1544, https://doi.org/10.1016/j.fuel.2019.05.147.

[29] X. Jiang, J. Yang, Y. Liang, H. Zhang, Y. Zhou, R. Shan, Q. Liu, W. Liu, L. Yao, In situ DRIFTS and DFT studies of SO_2 poisoning over Cu-exchanged X zeolite catalyst for NH_3-SCR, J. Environ. Chem. Eng. 11 (3) (2023) 109822, https://doi.org/10.1016/j.jece.2023.109822.

[30] H. Ming, D. Wei, Y. Yang, B. Chen, C. Yang, J. Zhang, Y. Hou, Photocatalytic activation of peroxymonosulfate by carbon quantum dots functionalized carbon nitride for efficient degradation of bisphenol A under visible-light irradiation, Chem. Eng. J. 424 (2021) 130296, https://doi.org/10.1016/j.cej.2021.130296.

[31] W. Yang, X. Chen, L. Chen, Y. Feng, C. Wu, X. Ding, Z. Gao, Y. Liu, H. Li, Design of single-atom catalysts for Hg^0 oxidation using H_2O_2, J. Phys. Chem. C. 126 (50) (2022) 21234–21242, https://doi.org/10.1021/acs.jpcc.2c06266.

[32] B. Wu, Y. Xiong, J. Ru, H. Feng, Enhancement of NO absorption in ammonium-based solution using heterogeneous Fenton reaction at low H_2O_2 consumption, Korean J. Chem. Eng. 33 (12) (2016) 3407–3416, https://doi.org/10.1007/s11814-016-0195-2.

[33] W. Yang, X. Liu, X. Chen, Y. Cao, S. Cui, L. Jiao, C. Wu, C. Chen, D. Fu, I.D. Gates, Z. Gao, H.L. Jiang, A sulfur-tolerant MOF-based single-atom Fe catalyst for efficient oxidation of NO and Hg^0, Adv. Mater. 34 (20) (2022) 2110123, https://doi.org/10.1002/adma.202110123.

[34] J. Yang, S. Ren, Y. zhou, Z. Su, L. Yao, J. Cao, L. Jiang, G. Hu, M. Kong, J. Yang, Q. Liu, In situ IR comparative study on N_2O formation pathways over different valence states manganese oxides catalysts during NH_3–SCR of NO, Chem. Eng. J. 397 (2020), https://doi.org/10.1016/j.cej.2020.125446.

[35] M. Wang, S. Ren, Y. Jiang, B. Su, Z. Chen, W. Liu, J. Yang, L. Chen, Insights into co-doping effect of Sm and Fe on anti-Pb poisoning of Mn-Ce/AC catalyst for low-temperature SCR of NO with NH_3, Fuel 319 (2022), https://doi.org/10.1016/j.fuel.2022.123763.

[36] R. Hao, Y. Mao, X. Mao, Z. Wang, Y. Gong, Z. Zhang, Y. Zhao, Cooperative removal of SO_2 and NO by using a method of UV-heat/H_2O_2 oxidation combined with NH_4OH-$(NH_4)_2SO_3$ dual-area absorption, Chem. Eng. J. 365 (2019) 282–290, https://doi.org/10.1016/j.cej.2019.02.059.

[37] R.G. Kadam, T. Zhang, D. Zaoralova, M. Medved, A. Bakandritsos, O. Tomanec, M. Petr, J. Zhu Chen, J.T. Miller, M. Otyepka, R. Zboril, T. Asefa, M.B. Gawande,

Single Co-atoms as electrocatalysts for efficient hydrazine oxidation reaction, Small 17 (16) (2021) 2006477, https://doi.org/10.1002/smll.202006477.

[38] L. Ma, J.-M. Zhang, K.-W. Xu, V. Ji, A first-principles study on gas sensing properties of graphene and Pd-doped graphene, Appl. Surf. Sci. 343 (2015) 121–127, https://doi.org/10.1016/j.apsusc.2015.03.068.

[39] L. Zhao, Y. Zhang, L.-B. Huang, X.-Z. Liu, Q.-H. Zhang, C. He, Z.-Y. Wu, L.-J. Zhang, J. Wu, W. Yang, L. Gu, J.-S. Hu, L.-J. Wan, Cascade anchoring strategy for general mass production of high-loading single-atomic metal-nitrogen catalysts, Nat. Commun. 10 (1) (2019) 1278, https://doi.org/10.1038/s41467-019-09290-y.

[40] B. Wu, S. Zhang, S. He, Y. Xiong, Follow-up mechanism study on NO oxidation with vaporized H_2O_2 catalyzed by Fe_2O_3 in a fixed-bed reactor, Chem. Eng. J. 356 (2019) 662–672, https://doi.org/10.1016/j.cej.2018.09.041.

[41] J. Yang, Y. Zhao, S. Liang, S. Zhang, S. Ma, H. Li, J. Zhang, C. Zheng, Magnetic iron–manganese binary oxide supported on carbon nanofiber ($Fe_{3-x}Mn_xO_4$/CNF) for efficient removal of Hg^0 from coal combustion flue gas, Chem. Eng. J. 334 (2018) 216–224, https://doi.org/10.1016/j.cej.2017.10.004.

[42] M. Xu, L. Chen, X. Cheng, X. Meng, Q. Jin, C. Zhu, J. Yang, H. Xu, Reduction of SO_2 into sulfur over Ce-based catalyst: performance optimizations and reaction mechanisms, J. Environ. Chem. Eng. 12 (5) (2024) 114064, https://doi.org/10.1016/j.jece.2024.114064.

[43] Y. Zhao, R. Hao, M. Qi, Integrative process of preoxidation and absorption for simultaneous removal of SO_2,NO and Hg^0, Chem. Eng. J. 269 (2015) 159–167, https://doi.org/10.1016/j.cej.2015.01.064.

[44] Z. Chen, S. Ren, M. Wang, J. Yang, L. Chen, W. Liu, Q. Liu, B. Su, Insights into samarium doping effects on catalytic activity and SO_2 tolerance of MnFeO catalyst for low-temperature NH_3-SCR reaction, Fuel 321 (2022), https://doi.org/10.1016/j.fuel.2022.124113.

[45] J. Li, J. Chang, S. Cheng, Z. Wang, Y. Zhao, B. Zhou, C. Ma, L. Zhang, T. Wang, Z. Song, New insights into the influence of SO_2 as an activator on the physicochemical properties of carbon materials and the influence of S-doping on SO_2 adsorption: experimental and density functional theory study, Chem. Eng. J. 474 (2023), https://doi.org/10.1016/j.cej.2023.145902.

[46] W. Yang, Y. Feng, X. Chen, C. Wu, F. Wang, Z. Gao, Y. Liu, X. Ding, H. Li, Understanding trends in the NO oxidation activity of single-atom catalysts, J. Environ. Chem. Eng. 10 (6) (2022) 108744, https://doi.org/10.1016/j.jece.2022.108744.

[47] Q. Guo, X.-F. Yu, K. Zhang, L. Xia, S. Liu, W. Zhang, Y. Du, H. Tang, Y. Peng, Z. Li, L. Duan, X. Yang, Atomically dispersed Co-Mn dual sites anchored in photoresponsive carbon nitride mediated peroxymonosulfate activation for elimination of petroleum hydrocarbon in water, Appl. Catal. B: Environ. 343 (2024) 123581, https://doi.org/10.1016/j.apcatb.2023.123581.

[48] J. Lai, P. Wang, Y. Ma, Z. Han, H. Fiedler, X. Lin, X. Li, Unveiling the competitive mechanism between SO_2 and PCDD/Fs on activated carbon adsorption, J. Environ. Chem. Eng. 12 (6) (2024) 114254, https://doi.org/10.1016/j.jece.2024.114254.

[49] R.C.C. Costa, F.C.C. Moura, J.D. Ardisson, J.D. Fabris, R.M. Lago, Highly active heterogeneous Fenton-like systems based on Fe^0/Fe_3O_4 composites prepared by controlled reduction of iron oxides, Appl. Catal. B: Environ. 83 (1-2) (2008) 131–139, https://doi.org/10.1016/j.apcatb.2008.01.039.

[50] W. Yang, Z. Gao, X. Liu, X. Li, X. Ding, W. Yan, Single-atom iron catalyst with single-vacancy graphene-based substrate as a novel catalyst for NO oxidation: a theoretical study, Catal. Sci. Technol. 8 (16) (2018) 4159–4168, https://doi.org/10.1039/c8cy01225c.

[51] L. Ling, P. Han, B. Wang, R. Zhang, Theoretical prediction of simultaneous removal efficiency of ZnO for H_2S and Hg^0 in coal gas, Chem. Eng. J. 231 (2013) 388–396, https://doi.org/10.1016/j.cej.2013.07.047.

[52] B. Li, X. Wang, Y. Wang, W. Wang, S. Zhou, S. Zhang, W. Li, S. Li, Revealing the promotional effect of Ce doping on the low-temperature activity and SO_2 tolerance of Ce/$FeVO_4$ catalysts in NH_3-SCR, J. Environ. Chem. Eng. 10 (3) (2022) 107588, https://doi.org/10.1016/j.jece.2022.107588.

[53] S. Yang, D. Xu, W. Yan, Y. Xiong, Effective NO and SO_2 removal from fuel gas with H_2O_2 catalyzed by Fe_3O_4/Fe^0/Fe_3C encapsulated in multi-walled carbon nanotubes, J. Environ. Chem. Eng. 9 (4) (2021) 105413, https://doi.org/10.1016/j.jece.2021.105413.

[54] P. Wang, L. Bu, L. Luo, Y. Wu, W. Zhang, S. Zhou, J.C. Crittenden, Unveiling the fates of nitro-transformation products in advanced oxidation process: a DFT-based kinetic model, Chem. Eng. J. 473 (2023) 145273, https://doi.org/10.1016/j.cej.2023.145273.

[55] W. Zhu, S. Ndayiragije, X. Zuo, X. Zhang, G. Wang, X. Wang, ZIF-8-derived single-atom Cu and N co-coordinated porous carbon as bifunctional material for SMX removal, J. Environ. Chem. Eng. 10 (3) (2022), https://doi.org/10.1016/j.jece.2022.107758.

[56] C. Zhu, Y. Nie, S. Zhao, Z. Fan, F. Liu, A. Li, Constructing surface micro-electric fields on hollow single-atom cobalt catalyst for ultrafast and anti-interference advanced oxidation, Appl. Catal. B: Environ. 305 (2022), https://doi.org/10.1016/j.apcatb.2021.121057.

[57] Y. Mao, J. Cheng, H. Guo, L. Qian, J. Tu, W. Yang, Acid-base bifunctional Fe-NC catalyst with Fe-N_4 and Fe nanoparticles active sites derived from Fe-doped ZIF-8 boosted microalgal lipid conversion, Appl. Surf. Sci. 634 (2023), https://doi.org/10.1016/j.apsusc.2023.157679.

[58] G. Henkelman, A. Arnaldsson, H. Jónsson, A fast and robust algorithm for Bader decomposition of charge density, Comput. Mater. Sci. 36 (3) (2006) 354–360, https://doi.org/10.1016/j.commatsci.2005.04.010.

[59] G. Henkelman, H. Jónsson, Improved tangent estimate in the nudged elastic band method for finding minimum energy paths and saddle points, J. Chem. Phys. 113 (22) (2000) 9978–9985, https://doi.org/10.1063/1.1323224.

[60] S. Grimme, J. Antony, S. Ehrlich, H. Krieg, A consistent and accurate ab initio parametrization of density functional dispersion correction (DFT-D) for the 94 elements H-Pu, J. Chem. Phys. 132 (15) (2010) 154104, https://doi.org/10.1063/1.3382344.

[61] L.I. Bendavid, E.A. Carter, CO_2 adsorption on $Cu_2O(111)$: a DFT+U and DFT-D Study, J. Phys. Chem. C. 117 (49) (2013) 26048–26059, https://doi.org/10.1021/jp407468t.

[62] C. Riplinger, E.A. Carter, Cooperative effects in water binding to cuprous oxide surfaces, J. Phys. Chem. C. 119 (17) (2015) 9311–9323, https://doi.org/10.1021/acs.jpcc.5b00383.

[63] W. Yang, H. Huang, X. Liu, J. Ren, K. Ma, Z. Pan, Z. Ding, X. Ding, Z. Gao, Screening the activity of single-atom catalysts for the catalytic oxidation of sulfur dioxide with a kinetic activity model, Chem. Commun. 56 (78) (2020) 11657–11660, https://doi.org/10.1039/d0cc05320a.

[64] A. Heyden, A.T. Bell, F.J. Keil, Efficient methods for finding transition states in chemical reactions: comparison of improved dimer method and partitioned rational function optimization method, J. Chem. Phys. 123 (22) (2005) 224101, https://doi.org/10.1063/1.2104507.

[65] G. Henkelman, B.P. Uberuaga, H. Jónsson, A climbing image nudged elastic band method for finding saddle points and minimum energy paths, J. Chem. Phys. 113 (22) (2000) 9901–9904, https://doi.org/10.1063/1.1329672.

[66] W. Yang, L. Chen, B. Zhou, Z. Jia, X. Liu, Y. Liu, H. Li, Z. Gao, NO oxidation using H_2O_2 at a single-atom iron catalyst, J. Phys. Chem. C. 127 (27) (2023) 13011–13020, https://doi.org/10.1021/acs.jpcc.3c01976.